Iron-Molybdenum Sulfide Electrocatalysts for the Hydrogen Evolution Reaction: An Operando XAS study

Anastassiya Khan, Adina Morozan, Hannah Johnson, Vincent Artero, Andrea Zitolo

Iron-Molybdenum Sulfide Electrocatalysts for the Hydrogen Evolution Reaction: An *Operando* XAS study

Anastassiya Khan[1], Adina Morozan[2], Hannah Johnson[3], Vincent Artero[2], Andrea Zitolo[1]*

[1]*Synchrotron SOLEIL, L'Orme des Merisiers, Départementale 128, 91190 Saint-Aubin, France*

[2]*Univ. Grenoble Alpes, CNRS, CEA, IRIG, Laboratoire de Chimie et Biologie des Métaux, 38054, Grenoble, France*

[3]*Toyota Motor Europe, Materials Engineering, Hoge Wei 33, Zaventem 1930, Belgium*

* To whom correspondence should be addressed:

* e-mail: andrea.zitolo@synchrotron-soleil.fr

Abstract

The comprehensive characterization of the structure-electrocatalytic activity relationships is of great interest to support the development of efficient catalysts for hydrogen evolution reaction (HER) in proton-exchange membrane (PEM) electrolyzers. The successful implementation of a bimetallic iron-molybdenum sulfide electrocatalyst for HER into a PEM electrolyzer has been reported. However, the precise nature of their active sites is still elusive. In this study, we employed X-ray absorption spectroscopy (XAS) to study iron-molybdenum and molybdenum sulfides obtained by a microwave irradiation synthetic approach. *Operando* XAS measurements in an acidic environment revealed sulfur-defective amorphous MoS_x and FeS phases. Although the amount of dopant Fe is 10 times lower than that of Mo, the synergy between the two phases promotes the HER performance of iron-molybdenum sulfides.

Keywords

Iron-molybdenum sulfide, hydrogen evolution reaction, electrocatalyst, X-ray absorption spectroscopy, operando

1. Introduction

In order to promote the transition to an energy system less dependent on fossil fuels, the study and deployment of new, emerging and clean energy technologies has substantially intensified in recent years [1-3]. Hydrogen has emerged as a highly promising renewable energy vector, distinguished by its unparalleled energy density per unit mass compared to all other fuels [4]. However, traditional industrial hydrogen production methods, such as steam reforming, rely on fossil fuels and result in significant CO_2 emissions, limiting their sustainability. In contrast, water electrolysis, if powered by renewable sources, presents a compelling solution for producing pure hydrogen without introducing greenhouse gases into the atmosphere [5-8].

Alkaline electrolyzers are already commercially available. However, the relatively high cost of hydrogen production has limited the uptake of this technology. A potential future approach to replace the commonly employed alkaline water electrolysis for industrial hydrogen production is the use of proton exchange membrane (PEM) electrolyzers working with acid-based solid electrolytes. This technology offers remarkable advantages compared to alkaline systems, such as exceptional power efficiency, significantly lower overvoltage, high current densities, reduced maintenance and less safety concerns [6, 9]. However, PEM devices commonly rely on expensive and scarce noble metal catalysts, which pose a barrier to their widespread implementation [10-12]. Therefore, finding non-noble metal alternatives for the hydrogen evolution reaction (HER) has become crucial to advance acidic water electrolysis, ensuring its affordability and scalability for practical applications.

Considering this perspective, many transition metal compounds [13, 14], including phosphides [15-17], carbides [18, 19], oxides [20, 21], nitrides [22], and selenides [23], have been thoroughly investigated as electrocatalysts for the HER, and among them, molybdenum disulfide (MoS_2) has garnered significant interest since the 1970s, when the HER activity of crystalline *c*-MoS_2 was first recognized [24]. However, the properties of MoS_2 in bulk form can substantially vary from those of its nanoscale counterparts. Indeed, extensive efforts are dedicated to the ongoing engineering of this material to optimize electrical conductivity, prevent material agglomeration, enhance stability, reduce reaction energy barriers, and boost the catalytic HER process. A plethora of state-of-the-art strategies have been employed to enhance MoS_2 performance: defect engineering [25], doping [26], phase engineering [27], hierarchical porous structuring [28-30], morphological control, i.e. synthesis of nanoparticles, single/few-layer nanosheets, nanodots, nanoflowers, nanobelts [31-35], and maximizing the exposure of highly active edge sites for HER [36]. To address the issue of poor intrinsic conductivity, extensive efforts have been made to utilize highly conductive substrates.

Notably, coupling with carbon materials (carbon black, carbon nanofibers, carbon nanotubes [37-41]) has proven effective in overcoming this challenge.

Beyond *c*-MoS_2, amorphous molybdenum sulfides (*a*-MoS_x) has recently gained attention thanks to its scalable preparation methods, attractive catalytic activities and robustness [42]. It was found that the electrocatalytic performance of both crystalline and amorphous molybdenum sulfides was significantly improved through the combination with other transition metal ions, such as in the case of nanostructured NiMoS [43], Co_9S_8@MoS2 core-shell nanostructures [44], V and Zn-doped MoS_2 [45, 46], and iron-promoted HER activity in Fe-MoS_3 [47], FeS_2-doped MoS_2 [48], and amorphous $FeMoS_4$ [49]. Our group succeeded in synthesizing an amorphous $FeMoS_x$ material through a novel microwave-assisted method. This material exhibits remarkable HER activity in acidic environments requiring an overpotential of ~150 mV to reach a current density of 10 mA cm^{-2}, while demonstrating stability during operation comparable to Pt, thus making it a promising candidate for utilization as a cathode catalyst in PEM electrolyzers [50].

Each of the strategies to optimize molybdenum sulfides involves a control and comprehensive understanding of the structural and electronic properties at the atomic and molecular levels. In particular, the need to correlate structural and electronic changes with the activity and stability of novel electrocatalysts requires the use of sophisticated *in-situ* and *operando* techniques. X-ray absorption spectroscopy (XAS) plays today a privileged role in the investigations of catalysts across a wide spectrum of experimental conditions [51]. With its element-specific ability, XAS proved to be an incomparable tool in isolating the active sites within complex, multi-element systems and can be employed to explore an extensive array of materials, including crystalline, amorphous, nanostructured, and liquid phases [52]. Lassalle et al. successfully applied XAS for the study of amorphous MoS_x under catalytic conditions [53]. Furthermore, through the utilization of *operando* XAS measurements, Wu et al. provided

experimental evidence of the crucial influence of a short Mo-Mo network in increasing the HER activity in 1T (octahedrally coordinated) and *a*-MoS_2 relative to the crystalline 2H (trigonally coordinated) MoS_2 [54].

In this study, we employed *operando* XAS to elucidate the structural basis for the improved catalytic performance of iron-doped and non-doped molybdenum sulfides prepared using the above-mentioned microwave synthesis method, and labelled $FeMoS_{mw}$ and MoS_{mw}. Our investigation revealed the presence of a sulfur-defective amorphous MoS_x phase in both compounds, with the additional identification of a sulfur-defective amorphous FeS phase in $FeMoS_x$ during operation. These findings demonstrate the active involvement of these species during HER, thus representing a significant advancement in the comprehension and development of molybdenum sulfides-based electrocatalysts for water-splitting applications.

2. Experimental section

2.1 Synthesis of $FeMoS_{mw}$ and MoS_{mw}

The synthesis of iron-molybdenum sulfide materials involved the use of thiourea, Fe and Mo salts ($MoCl_3$ and $FeCl_3{\cdot}H_2O$) in a molar ratio of 3:1:1. In this process, metal salts and thiourea were mixed in ethylene glycol and ethanol, leading to the formation of metal-thiourea complexes. Under microwave irradiation (0-300 W, 255 °C, 8 bar), these complexes underwent decomposition, resulting in the formation of iron-molybdenum sulfide labeled as $FeMoS_{mw}$. For comparison, a sample was prepared similarly but without the Fe precursor and referred to as MoS_{mw}. Further details on the synthesis of $FeMoS_{mw}$ and MoS_{mw} samples can be found in reference [50]. MoS_2 (99%) and MoS_3 (97 %) were purchased from Sigma-Aldrich and Alfa-Aesar, respectively.

2.2 Electrochemical measurements

Electrochemical activity of the catalyst toward the HER was determined using a glassy carbon disk (⌀ 3 mm, 0.07 cm^2, catalyst loading of 0.82 $mg \cdot cm^{-2}$) as working electrode. A catalyst ink including 1 mg of electrocatalyst, 160 μL of ethanol, 40 μL of water, 10 μL of 5 wt % Nafion solution, and 0.2 mg of carbon nanotubes (CNTs) was prepared by sonication.

The electrochemical experiments were performed in a N_2-saturated electrolyte (0.1 M H_2SO_4), in a three-electrode cell configuration and using an SP300 Bio-Logic potentiostat. The counter electrode consisted of a Ti wire, and the reference electrode was a Ag/AgCl, KCl (3 M). All curves were iR-corrected by carrying out automatically ohmic drop compensation by the EC-Lab software using the electrochemical impedance technique (ZIR).

2.3 XAS data collection and analysis

Mo and Fe K-edge X-ray absorption spectra were collected at room temperature at the SAMBA beamline (Synchrotron SOLEIL). The beamline is equipped with a sagittaly focusing Si 220 monochromator and two Pd-coated collimating/focusing mirrors, used to remove X-rays harmonics. The spectra of the reference compounds MoS_2 and MoS_3 were recorded in transmission mode, while the catalysts data collection was performed in fluorescence mode, using a Canberra 35-elements monolithic planar Ge pixel array detector. For *operando* XAS measurements, catalysts inks were prepared by ultrasonication of a mixture of 10 mg of catalysts, 2 mg of CNTs, 100 ml of 5% Nafion solution, 50 μl of water and 1 ml of ethanol for 20 minutes. An aliquot was then dropcasted on a 100 μm graphite foil (Goodfellow cat. C 000200/2), and installed in a three-electrode electrochemical cell [55], using a Pt counter electrode, a saturated calomel reference electrode, and 0.1 M H_2SO_4 N_2-saturated electrolyte.

The EXAFS data analysis was performed with the GNXAS code, which is based on the decomposition of the EXAFS $\chi(k)$ signal into a summation over n-body distribution functions $\gamma(n)$ calculated by means of the multiple-scattering (MS) theory. Details of the theoretical framework of the GNXAS approach are described in refs [56, 57]. The Mo and Fe coordination shells have been modelled with Γ-like distribution functions which depend on four parameters, namely, the coordination number N, the average distance R, the mean-square variation σ^2, and the skewness β. Additional nonstructural parameters were minimized, namely E_0 (core ionization threshold energy) and S_0^2, therefore taking into account the maximum number of independent parameters according to the rule $N_{max} = 2\Delta R\Delta k/\pi$ (Δk: total range in k space, R: total range in ΔR space) [58].

3. Results

3.1 Electrochemical measurements

Both $FeMoS_{mw}$ and MoS_{mw} were tested for the H_2 evolution reaction in 0.1 M aqueous H_2SO_4 solution of pH 1. To ensure a good contact with the glassy-carbon electrode and optimize the surface area in contact with the electrolyte, they were formulated in an ink containing CNTs and Nafion. Polarization curves are shown in Figure 1. The $FeMoS_{mw}$ catalyst mediates H_2 evolution at potentials more negative than -0.10 V vs RHE with a current density of 10 $mA{\cdot}cm^{-2}$ obtained at -0.15 V vs RHE. The MoS_{mw} sample displays a slighly more negative onset potential and reaches 10 $mA{\cdot}cm^{-2}$ at -0.2 V vs. RHE.

3.2 Ex-situ identification of MoS_x phase: Mo K-edge XAS analysis

The comparison between the X-ray absorption near edge structure (XANES) spectrum of MoS_{mw} and the MoS_2 and MoS_3 reference compounds, shown in Figure S1a, reveals spectral features similar to those of MoS_3. Furthermore, the position of the absorption edge in a XANES spectrum is a function of the oxidation state of the photo-absorbing element. It can

be observed that the absorption edge of the MoS_{mw} XANES spectrum coincides with that of the reference MoS_3, thereby allowing the same valence state to be attributed to both compounds. The Fourier transformed extended X-ray absorption fine structure (FT-EXAFS) spectra of MoS_{mw} is showed in Figure S1b and compared with those of the MoS_2 and MoS_3 reference compounds. The spectrum of MoS_{mw} is similar to that of MoS_3, allowing us to identify the phase present in our catalyst as MoS_3. However, the first-shell peak corresponding to the Mo-S distance, and located at about 1.9 Å (not-corrected for the phase-shift) for MoS_3, is shifted to lower values for MoS_{mw} (about 1.84 Å).

There are still open questions regarding the structure and electronic properties of amorphous molybdenum sulfide, which is described based on two models: the Hibble model [59] and the Weber model [60]. In the Hibble model, the structure of *a*-MoS_3 consists of a chain configuration, in which the Mo atoms are bridged by three sulfides (S^{2-}) or by one sulfide and one disulfide (S_2^{2-}) ligand (Figure 2a). The formula for this model is $Mo^{5+}(S^{2-})_2(S_2^{2-})_{0.5}$. The Weber model, consists of triangular Mo_3S_9 clusters, which are connected to each other by sulfide bridges and whose formula is $Mo^{4+}(S^{2-})(S_2^{2-})$ (Figure 2b). More recently, Tran, Artero and colleagues proposed a model based on clusters of $[Mo_3S_{13}]^{2-}$ sharing two of their terminal disulfide groups (Figure 2c) [61]. These structures can contain three main types of sulfur atoms: bridging S_2^{2-} (a pair of sulfur atoms bonded to two molybdenum atoms), terminal S_2^{2-} (a pair of sulfur atoms bonded to one molybdenum atom), and apical S^{2-} (a sulfur atom bonded to three molybdenum atoms). There is currently a debate about the activity of these different types of S atoms. For example, through a combined study using XPS, DFT calculations, and in-situ Raman spectroscopy, Ting et al. shown that bridging S_2^{2-} have greater activity than terminal S_2^{2-} in amorphous MoS_x, while apical S^{2-} absorbs hydrogen too weakly to catalyze the HER reaction [62]. On the contrary, Lassalle et al. suggest an involvement of terminal disulfides in the hydrogen evolution mechanism [53]. Tran et al. further suggest that

the activity of *a*-MoS_x is not due to S sites, but rather to Mo sites: once the HER potential is reached, the terminal disulfide is eliminated, followed by the formation of Mo-H, as the active site for the HER reaction [61].

Although these proposed structures are indistinguishable from an EXAFS point of view, the analysis of the EXAFS spectral region can reveal accurate structural information that is useful for understanding possible deviations from reference compounds.

The best fit analysis of the MoS_{mw} EXAFS spectrum is shown in Figure 3a and S2a, while the structural parameters obtained from the fitting procedure are reported in Table 1. For comparison, we also included in Table 1 the structural parameters obtained from the analysis of the MoS_3 reference spectrum (Figure S3). Our EXAFS analysis of MoS_{mw} revealed the presence of Mo-S bonds at 2.37 Å with a coordination number (CN) of 3.5, one Mo-Mo interaction at 2.76 Å, and Mo-O bond at 1.68 Å with a CN of 0.2. The Mo-O contribution was necessary to achieve a good agreement between the experimental and calculated spectra, and it is consistent with our previous XPS measurements performed on the same sample [50] and with previous EXAFS analyses on amorphous MoS_x films [53]. The Mo-S and Mo-Mo bond distances obtained from the fitting procedure are in good agreement with the values determined from EXAFS studies on *a*-MoS_3 [53, 59, 63]. However, the coordination number of Mo-S is lower compared to that of the reference compound (3.5 instead of 5.6). This is due to the presence of Mo-O contributions, which decrease the average Mo-S bonds per Mo centre.

Figure S4 shows the comparison between the experimental XANES and FT-EXAFS spectra of $FeMoS_{mw}$ and MoS_{mw}. The XAS spectra of the two compounds are the identical in all the spectral range (any differences in the oscillations of the FT-EXAFS spectra above 3 Å may be due to very week signals or experimental noise), demonstrating that iron-molybdenum sulfide and molybdenum sulfide obtained by microwave synthesis, have the same MoS_x phase.

Indeed, the results of the EXAFS best-fit for $FeMoS_{mw}$ shows a set of structural parameters that are, within the statistical errors, identical to those of MoS_{mw} (Table 1, Figure 3b and S2b). Note that the high values of the Debye Waller factors for the Mo-S and Mo-Mo distances confirm the amorphous nature of the MoS_3 phase in both MoS_{mw} $FeMoS_{mw}$.

3.3 Operando Mo K-edge XAS signatures

We then investigated the behavior of MoS_{mw} and $FeMoS_{mw}$ under *operando* conditions. Figure 4a shows the Mo K-edge XANES spectra of MoS_{mw} recorded for the dry electrode, at OCP potential, and at -0.21V vs RHE in acidic media, and Figure 4b shows the same comparison for $FeMoS_{mw}$. The XANES spectra of MoS_{mw} in the dry state and at OCP are almost identical, while a change occurs when applying a working potential in the region corresponding to the first minimum at about 20055 eV, and an increase in the shoulder around 20014 eV. The spectra of $FeMoS_{mw}$ shows the same spectral changes as soon as the electrode comes into contact with the electrolyte. This effect has been attributed to the dissolution of the oxide layer present on the surface [53]. This hypothesis was confirmed through the quantitative analysis of the EXAFS spectra of MoS_{mw} and $FeMoS_{mw}$ (Figures S5 and S6, Table 1). In the case of MoS_{mw} at OCP the best-fit was still obtained including a Mo-O contribution, while for $FeMoS_{mw}$, in the presence of the electrolyte, the Mo-O signal is no longer detectable from the EXAFS analysis. This is line with the fact that no pre-wave corresponding to the reduction of molybdenum oxide is observed during linear scan voltammetry experiments with $FeMoS_{mw}$ (see Figure S7), by contrast to MoS_{mw}, and indicates that such Mo-O functions are readily reduced during equilibration of $FeMoS_{mw}$ samples at OCP. In both MoS_{mw} and $FeMoS_{mw}$, under catalytic conditions, the surface is free of Mo-O contributions. The effect of removing the surface oxide ligands is also evident from the change in the coordination number of the Mo-S contribution: for MoS_{mw}, the CN increases

from 3.5 in the dry electrode to 3.8 at OCP and 4.7 at -0.21V vs RHE, while for $FeMoS_{mw}$ it increases from 3.3 in the dry electrode to 3.9 at OCP and 4.3 at -0.21V vs RHE. This means that, due to the disappearance of the Mo-O signal, the average number of S atoms per Mo centre increases, although it does not reach the value of 5.6 of the *a*-MoS_3 reference compound, thus identifying a sulfur-defective geometry even under catalytic conditions. Another important information that can be determined from the *operando* XAS measurements is that the spectra of MoS_{mw} and $FeMoS_{mw}$ under applied potential are identical (see Figure S8). This result demonstrates that under working conditions the amorphous molybdenum sulfide and iron-doped molybdenum sulfide have the same MoS_x phase. This result is surprising because the introduction of iron does not alter the structure of *a*-MoS_3, although it promotes the HER activity of amorphous MoS_x.

3.4 Ex-situ and Operando Fe K-edge XAS signatures

Figure 5a shows the comparison between the Fe K-edge XANES spectra of $FeMoS_{mw}$ for the dry electrode and at OCP potential in acidic media, while Figure 5b shows the same spectra in the Fourier transformed EXAFS space. This comparison identifies the presence of two different phases between the dry electrode and the one in contact with the electrolyte: indeed, the XANES spectrum of the $FeMoS_{mw}$ dry electrode shows a more pronounced white line and a 1.1 eV positive shift in the absorption edge compared to the spectrum at OCP (Figure 5a, and Figure S9 showing the comparison between the first derivative of the XAS spectra of $FeMoS_{mw}$ dry electrode and at OCP, used for the determination of the edge position, E_0). This is generally attributable to the coordination of Fe with oxygenated species, which also increases the iron valence. The FT-EXAFS spectra also show a difference in the position of the first shell peak of $FeMoS_{mw}$ dry electrode, located at about 1.64 Å (not-corrected for the phase-shift), while that at OCP is located at about 1.76 Å (Figure 5b).

The presence of bubbles formed during catalytic conditions does not allow for a long-range extraction of the EXAFS signal above *k* 7.5 for $FeMoS_{mw}$ at -0.21V vs RHE. However, the comparison of the XANES spectra of $FeMoS_{mw}$ at OCP and at -0.21V vs RHE, and the EXAFS spectra up to *k* 7.5, shows identical spectral features, demonstrating the presence of the same phase both at OCP and under working conditions (Figure S10). Therefore, the spectrum of $FeMoS_{mw}$ at OCP can be considered representative of the species present in the catalytic state and used for an accurate structural analysis. The best-fit EXAFS analysis of $FeMoS_{mw}$ dry electrode is shown in Figure 6a and S11a, while the corresponding structural parameters obtained are reported in Table 2. The spectrum can be correctly reproduced with Fe-S and Fe-O contributions at 2.28 and 2.02 Å, and an Fe-Fe contribution at 2.86 Å. The Fe-O signal identifies the presence of iron oxide, while the Fe-S distance is in agreement with a previous EXAFS determination of amorphous iron sulfide *a*-FeS [64]. Once in contact with the electrolyte, the iron oxide is hydrolyzed, and during the catalytic state the only phase present is *a*-FeS (Figure 6b and S11b and Table 2). Indeed, the EXAFS analysis identifies the presence of only Fe-S first shell contributions. It is noteworthy that the dissolution of iron oxide leads to an increase in the coordination number of the Fe-S distance, from 0.6 to 2.7, much closer to the value of 4 found for *a*-FeS [64], but still identifying a coordinatively sulfur-deficient structure.

4. Discussion and Conclusions

Raman and XRD studies revealed an amorphous nature for both $FeMoS_{mw}$ and MoS_{mw} [50], making it necessary to employ a structural technique like XAS, capable of identifying the local structure of a compound even in the amorphous phase and its evolution under reaction conditions. Moreover, the high sensitivity of XAS in detecting small amounts of chemical species makes it particularly attractive in the case of $FeMoS_{mw}$, as ICP-AES measurements

revealed an iron content approximately 10 times lower than that of molybdenum, with a chemical composition expressed as $Fe_{0.11}Mo_{1.14}S_2$ [50]. XPS has been an extremely useful technique that has allowed us to identify the presence of MoS_x, MoO_x, and FeS_x species [50]. However, this technique is capable of probing only the surface, was not applied under real catalytic conditions and does not possess the accuracy of XAS in investigating the local structural geometry of the materials of interest.

The analysis of the ex-situ XAS spectra allowed us to identify the same *a*-MoS_3 phase in both $FeMoS_{mw}$ and MoS_{mw}. We identified a *a*-MoS_3 sulfur-defective geometry, whose Mo-Mo bond distance exhibits a greater degree of disorder compared to bulk *a*-MoS_3, highlighting the structural complexity of various forms of *a*-MoS_3 that can be obtained by different synthesis pathways and their impact on HER reactivity. Through a DFT study and comparison with EXAFS, infrared spectroscopy, and XPS results, A. Sahu et al. has indeed shown the possible existence of *a*-MoS_3 polymorphs that can be generated under different experimental conditions [65]. One of the most interesting aspects revealed by *operando* XAS is that both $FeMoS_{mw}$ and MoS_{mw} maintain the same MoS_x amorphous phase, without it undergoing changes under catalytic conditions. On the one hand, therefore, doping with iron does not alter the structure and electronic properties of MoS_x, but it increases the HER performance of $FeMoS_{mw}$. Understanding the origin of this difference in activity between $FeMoS_{mw}$ and MoS_{mw} was possible by studying the *operando* XAS spectra of $FeMoS_{mw}$ at the Fe K-edge. The analysis of $FeMoS_{mw}$ under ex-situ conditions identified the presence of two phases, *a*-FeS and FeO_x, although under catalytic conditions, only *a*-FeS is present. FeS-base catalysts have also been reported to possess HER activity. For example, Zhang et al. synthesized amorphous $Fe_{0.95}S_{1.05}$ by solvothermal method exhibiting excellent HER performance in acidic media, with a low overpotential of 67 mV (current density of 10 $mA \cdot cm^{-2}$) compared to Pt [66], while Zhou et al. reported a high HER activity of FeS nanosheets triggered by near

infrared radiation [67]. $FeMoS_{mw}$ requires ~150 mV overpotential to reach 10 $mA \cdot cm^{-2}$, which is 30 mV less than shown by MoS_{mw}. Therefore, the origin of an increased efficiency of $FeMoS_{mw}$ compared to MoS_{mw} can be attributed to the presence of a sulfur-defective amorphous phase of FeS. This is a surprising result, as the amount of Fe is 10 times lower than that of Mo. From a spectroscopic point of view, XAS measurements do not show any direct interaction between *a*-FeS and *a*-MoS_3, but we cannot exclude a synergistic effect between the two phases, and an effect of *a*-FeS on the electronic properties of *a*-MoS_3 and its active sites. Indeed, theoretical studies have predicted that doping metal di-chalcogenides with transition metals enhances their electrical properties, resulting in a charge transfer from the metal d-orbitals [68]. Thus, modifying the electronic structure of molybdenum sulfides through metal atom doping could be crucial for optimizing hydrogen adsorption energy and promoting the Volmer-Tafel and/or the Volmer-Heyrovsky step [69]. Also, doping at the Mo-sites with Fe (and other elements like Co, Ni, Cu, Zn) can improve the activity of S-edge sites [70-72]. We believe that these results can pave the route for further computational explorations, capable of highlighting the synergistic effects of the two phases, *a*-FeS and *a*-MoS_3, by identifying the role of the active sites and their catalytic mechanisms.

From a broader perspective, this study outcomes provide new elements in understanding the structure-activity relationship of metal-doped molybdenum sulfides, and can significantly contribute to developing new models to unveil and predict the HER mechanisms in this class of materials, through both spectroscopic and theoretical approaches.

Acknowledgments

We would like to acknowledge Prof. Elena Savinova, whose pioneering studies have profoundly inspired the scientific community in the challenging task of elucidating the intricate relationship between the structure and activity of electrocatalytic materials. Despite

the remarkable achievements of women in science, they still represent only 33% of researchers globally. We are especially grateful for Prof. Savinova's strong commitment to science and education, which has made her a role model for future generations of researchers, particularly young women aspiring to pursue scientific careers and break the glass ceiling.

We acknowledge support from the French ANR projects ANR-19-CE05-0006 (SPECTROSCOPE), ANR-17-EURE-0003 (Labex ARCANE, CBH-EUR-GS) for funding, and Synchrotron SOLEIL (Gif-sur Yvette, France) for provision of synchrotron radiation facilities at beamline SAMBA.

References:

[1] A. Bartolini, F. Carducci, C.B. Muñoz, G. Comodi, Energy storage and multi energy systems in local energy communities with high renewable energy penetration, Renewable Energy, 159 (2020) 595-609.
[2] H.H. Pourasl, R.V. Barenji, V.M. Khojastehnezhad, Solar energy status in the world: A comprehensive review, Energy Reports, 10 (2023) 3474-3493.
[3] S. Nagireddi, J.R. Agarwal, D. Vedapuri, Carbon Dioxide Capture, Utilization, and Sequestration: Current Status, Challenges, and Future Prospects for Global Decarbonization, ACS Engineering Au, 4 (2024) 22-48.
[4] L. Schlapbach, A. Züttel, Hydrogen-storage materials for mobile applications, Nature, 414 (2001) 353-358.
[5] A. Buttler, H. Spliethoff, Current status of water electrolysis for energy storage, grid balancing and sector coupling via power-to-gas and power-to-liquids: A review, Renewable and Sustainable Energy Reviews, 82 (2018) 2440-2454.
[6] S. Shiva Kumar, V. Himabindu, Hydrogen production by PEM water electrolysis – A review, Materials Science for Energy Technologies, 2 (2019) 442-454.
[7] X. Tao, Y. Zhao, S. Wang, C. Li, R. Li, Recent advances and perspectives for solar-driven water splitting using particulate photocatalysts, Chemical Society Reviews, 51 (2022) 3561-3608.
[8] M. Chatenet, B.G. Pollet, D.R. Dekel, F. Dionigi, J. Deseure, P. Millet, R.D. Braatz, M.Z. Bazant, M. Eikerling, I. Staffell, P. Balcombe, Y. Shao-Horn, H. Schäfer, Water electrolysis: from textbook knowledge to the latest scientific strategies and industrial developments, Chemical Society Reviews, 51 (2022) 4583-4762.
[9] M. Carmo, D.L. Fritz, J. Mergel, D. Stolten, A comprehensive review on PEM water electrolysis, International Journal of Hydrogen Energy, 38 (2013) 4901-4934.
[10] C. Rozain, E. Mayousse, N. Guillet, P. Millet, Influence of iridium oxide loadings on the performance of PEM water electrolysis cells: Part I–Pure IrO2-based anodes, Applied Catalysis B: Environmental, 182 (2016) 153-160.
[11] B. Liu, C. Wang, Y. Chen, Surface determination and electrochemical behavior of IrO2-RuO2-SiO2 ternary oxide coatings in oxygen evolution reaction application, Electrochimica Acta, 264 (2018) 350-357.
[12] C. Li, J.-B. Baek, Recent Advances in Noble Metal (Pt, Ru, and Ir)-Based Electrocatalysts for Efficient Hydrogen Evolution Reaction, ACS Omega, 5 (2020) 31-40.

[13] M. Zeng, Y. Li, Recent advances in heterogeneous electrocatalysts for the hydrogen evolution reaction, Journal of Materials Chemistry A, 3 (2015) 14942-14962.
[14] A. Eftekhari, Electrocatalysts for hydrogen evolution reaction, International Journal of Hydrogen Energy, 42 (2017) 11053-11077.
[15] J.M. McEnaney, J.C. Crompton, J.F. Callejas, E.J. Popczun, A.J. Biacchi, N.S. Lewis, R.E. Schaak, Amorphous Molybdenum Phosphide Nanoparticles for Electrocatalytic Hydrogen Evolution, Chemistry of Materials, 26 (2014) 4826-4831.
[16] Z.W. Rui Zhang, Gaoyang Ye,Guanjie Chen,Jiaojiao Miao,Xuehua Zhou,Xiangwei Zhu,Xiaoqun Cao,Xiangnan Sun, “d-Electron Complementation” Induced V-Co Phosphide for Efficient Overall Water Splitting, Advanced Energy Materials, 11 (2021) 2101758.
[17] T. Liu, P. Li, N. Yao, G. Cheng, S. Chen, W. Luo, Y. Yin, CoP-Doped MOF-Based Electrocatalyst for pH-Universal Hydrogen Evolution Reaction, Angewandte Chemie International Edition, 58 (2019) 4679-4684.
[18] O. Rabi, E. Pervaiz, R. Zahra, M. Ali, M.B.K. Niazi, An inclusive review on the synthesis of molybdenum carbide and its hybrids as catalyst for electrochemical water splitting, Molecular Catalysis, 494 (2020) 111116.
[19] C. Tang, H. Zhang, K. Xu, Q. Zhang, J. Liu, C. He, L. Fan, T. Asefa, Unconventional molybdenum carbide phases with high electrocatalytic activity for hydrogen evolution reaction, Journal of Materials Chemistry A, 7 (2019) 18030-18038.
[20] J. Ampurdanés, M. Chourashiya, A. Urakawa, Cobalt oxide-based materials as non-PGM catalyst for HER in PEM electrolysis and in situ XAS characterization of its functional state, Catalysis Today, 336 (2019) 161-168.
[21] Y. Wu, R. Sun, J. Cen, Facile Synthesis of Cobalt Oxide as an Efficient Electrocatalyst for Hydrogen Evolution Reaction, Frontiers in Chemistry, 8 (2020).
[22] X. Peng, C. Pi, X. Zhang, S. Li, K. Huo, P.K. Chu, Recent progress of transition metal nitrides for efficient electrocatalytic water splitting, Sustainable Energy & Fuels, 3 (2019) 366-381.
[23] X. Xia, L. Wang, N. Sui, V.L. Colvin, W.W. Yu, Recent progress in transition metal selenide electrocatalysts for water splitting, Nanoscale, 12 (2020) 12249-12262.
[24] C.J.B. H. Tributsch, Electrochemistry and photochemistry of MoS2 layer crystals, J. Electroanal. Chem, 81 (1976) 97–111.
[25] L. Li, Z. Qin, L. Ries, S. Hong, T. Michel, J. Yang, C. Salameh, M. Bechelany, P. Miele, D. Kaplan, M. Chhowalla, D. Voiry, Role of Sulfur Vacancies and Undercoordinated Mo Regions in MoS(2) Nanosheets toward the Evolution of Hydrogen, ACS Nano, 13 (2019) 6824-6834.
[26] X. Zhang, Z. Feng, S. Zhang, Y. Liang, R. Wang, Engineering MoS2 Basal Planes for Hydrogen Evolution via Synergistic Ruthenium Doping and Nanocarbon Hybridization, Advanced Science, 6 (2019) 1900090.
[27] D. Wang, X. Zhang, S. Bao, Z. Zhang, H. Fei, Z. Wu, Phase engineering of a multiphasic 1T/2H MoS2 catalyst for highly efficient hydrogen evolution, Journal of Materials Chemistry A, 5 (2017) 2681-2688.
[28] Z. Lu, H. Zhang, W. Zhu, X. Yu, Y. Kuang, Z. Chang, X. Lei, X. Sun, In situ fabrication of porous MoS2 thin-films as high-performance catalysts for electrochemical hydrogen evolution, Chemical Communications, 49 (2013) 7516-7518.
[29] J. Zhu, Z.-C. Wang, H. Dai, Q. Wang, R. Yang, H. Yu, M. Liao, J. Zhang, W. Chen, Z. Wei, N. Li, L. Du, D.-X. Shi, W. Wang, L. Zhang, Y. Jiang, G. Zhang, Boundary activated hydrogen evolution reaction on monolayer MoS2, Nature Communications, 10 (2019).
[30] A. Wu, C. Tian, H. Yan, Y. Jiao, Q. Yan, G. Yang, H. Fu, Hierarchical MoS2@MoP core–shell heterojunction electrocatalysts for efficient hydrogen evolution reaction over a broad pH range, Nanoscale, 8 (2016) 11052-11059.
[31] X. Geng, W. Sun, W. Wu, B. Chen, A. Al-Hilo, M. Benamara, H. Zhu, F. Watanabe, J. Cui, T.-p. Chen, Pure and stable metallic phase molybdenum disulfide nanosheets for hydrogen evolution reaction, Nature Communications, 7 (2016) 10672.

[32] E. Heydari-Bafrooei, S. Askari, Electrocatalytic activity of MWCNT supported Pd nanoparticles and MoS2 nanoflowers for hydrogen evolution from acidic media, International Journal of Hydrogen Energy, 42 (2017) 2961-2969.
[33] C. Tan, Z. Luo, A. Chaturvedi, Y. Cai, Y. Du, Y. Gong, Y. Huang, Z. Lai, X. Zhang, L. Zheng, X. Qi, M.H. Goh, J. Wang, S. Han, X.-J. Wu, L. Gu, C. Kloc, H. Zhang, Preparation of High-Percentage 1T-Phase Transition Metal Dichalcogenide Nanodots for Electrochemical Hydrogen Evolution, Advanced Materials, 30 (2018) 1705509.
[34] X. Yin, Y. Yan, M. Miao, K. Zhan, P. Li, J. Yang, B. Zhao, B.Y. Xia, Quasi-Emulsion Confined Synthesis of Edge-Rich Ultrathin MoS2 Nanosheets/Graphene Hybrid for Enhanced Hydrogen Evolution, Chemistry, 24 3 (2018) 556-560.
[35] L. Yang, H. Hong, Q. Fu, Y. Huang, J. Zhang, X. Cui, Z. Fan, K. Liu, B. Xiang, Single-Crystal Atomic-Layered Molybdenum Disulfide Nanobelts with High Surface Activity, ACS Nano, 9 (2015) 6478-6483.
[36] T.F. Jaramillo, K.P. Jørgensen, J. Bonde, J.H. Nielsen, S. Horch, I. Chorkendorff, Identification of Active Edge Sites for Electrochemical H2 Evolution from MoS2 Nanocatalysts, Science, 317 (2007) 100-102.
[37] Y. Hyeon, S.-H. Jung, W. Jang, M. Kim, B.-S. Kim, J.-H. Lee, K.R. Nandanapalli, N. Jung, D. Whang, Unraveling the Factors Affecting the Electrochemical Performance of MoS2–Carbon Composite Catalysts for Hydrogen Evolution Reaction: Surface Defect and Electrical Resistance of Carbon Supports, ACS Applied Materials & Interfaces, 11 (2019) 5037-5045.
[38] P. Cao, J. Peng, J. Li, M. Zhai, Highly conductive carbon black supported amorphous molybdenum disulfide for efficient hydrogen evolution reaction, Journal of Power Sources, 347 (2017) 210-219.
[39] D.H. Youn, S. Han, J.Y. Kim, J.Y. Kim, H. Park, S.H. Choi, J.S. Lee, Highly Active and Stable Hydrogen Evolution Electrocatalysts Based on Molybdenum Compounds on Carbon Nanotube–Graphene Hybrid Support, ACS Nano, 8 (2014) 5164-5173.
[40] Y. Jiang, X. Li, S. Yu, L. Jia, X. Zhao, C. Wang, Reduced Graphene Oxide-Modified Carbon Nanotube/Polyimide Film Supported MoS2 Nanoparticles for Electrocatalytic Hydrogen Evolution, Advanced Functional Materials, 25 (2015) 2693-2700.
[41] M. Du, M. Zhang, M. Zou, T. Yang, S. Wang, J. Yao, B. Guo, S-rich single-layered MoS2 nanoplates embedded in N-doped carbon nanofibers: Efficient co-electrocatalysts for the hydrogen evolution reaction, Chem. Commun., 50 (2014).
[42] C. Chang, L. Wang, L. Xie, W. Zhao, S. Liu, Z. Zhuang, S. Liu, J. Li, X. Liu, Q. Zhao, Amorphous molybdenum sulfide and its Mo-S motifs: Structural characteristics, synthetic strategies, and comprehensive applications, Nano Research, 15 (2022) 8613-8635.
[43] J. Miao, F.-X. Xiao, H.B. Yang, S.Y. Khoo, J. Chen, Z. Fan, Y.-Y. Hsu, H.M. Chen, H. Zhang, B. Liu, Hierarchical Ni-Mo-S nanosheets on carbon fiber cloth: A flexible electrode for efficient hydrogen generation in neutral electrolyte, Science Advances, 1 e1500259.
[44] H. Zhu, J. Zhang, R. Yanzhang, M. Du, Q. Wang, G. Gao, J. Wu, G. Wu, M. Zhang, B. Liu, J. Yao, X. Zhang, When Cubic Cobalt Sulfide Meets Layered Molybdenum Disulfide: A Core–Shell System Toward Synergetic Electrocatalytic Water Splitting, Advanced Materials, 27 (2015) 4752-4759.
[45] S. Bolar, S. Shit, J.S. Kumar, N.C. Murmu, R.S. Ganesh, H. Inokawa, T. Kuila, Optimization of active surface area of flower like MoS2 using V-doping towards enhanced hydrogen evolution reaction in acidic and basic medium, Applied Catalysis B: Environmental, 254 (2019) 432-442.
[46] Y. Shi, Y. Zhou, D.-R. Yang, W.-X. Xu, C. Wang, F.-B. Wang, J.-J. Xu, X.-H. Xia, H.-Y. Chen, Energy Level Engineering of MoS2 by Transition-Metal Doping for Accelerating Hydrogen Evolution Reaction, Journal of the American Chemical Society, 139 (2017) 15479-15485.
[47] D. Merki, H. Vrubel, L. Rovelli, S. Fierro, X. Hu, Fe, Co, and Ni ions promote the catalytic activity of amorphous molybdenum sulfide films for hydrogen evolution, Chemical Science, 3 (2012) 2515-2525.
[48] X. Zhao, X. Ma, Q. Lu, Q. Li, C. Han, Z. Xing, X. Yang, FeS2-doped MoS2 nanoflower with the dominant 1T-MoS2 phase as an excellent electrocatalyst for high-performance hydrogen evolution, Electrochimica Acta, 249 (2017) 72-78.

[49] X. Ren, W. Wang, R. Ge, S. Hao, F. Qu, G. Du, A.M. Asiri, Q. Wei, L. Chen, X. Sun, An amorphous FeMoS4 nanorod array toward efficient hydrogen evolution electrocatalysis under neutral conditions, Chemical Communications, 53 (2017) 9000-9003.
[50] A. Morozan, H. Johnson, C. Roiron, G. Genay, D. Aldakov, A. Ghedjatti, C.T. Nguyen, P.D. Tran, S. Kinge, V. Artero, Nonprecious Bimetallic Iron–Molybdenum Sulfide Electrocatalysts for the Hydrogen Evolution Reaction in Proton Exchange Membrane Electrolyzers, ACS Catalysis, 10 (2020) 14336-14348.
[51] J. Timoshenko, B. Roldan Cuenya, In Situ/Operando Electrocatalyst Characterization by X-ray Absorption Spectroscopy, Chemical Reviews, 121 (2021) 882-961.
[52] A. Iglesias-Juez, G.L. Chiarello, G.S. Patience, M.O. Guerrero-Pérez, Experimental methods in chemical engineering: X-ray absorption spectroscopy—XAS, XANES, EXAFS, The Canadian Journal of Chemical Engineering, 100 (2022) 3-22.
[53] B. Lassalle-Kaiser, D. Merki, H. Vrubel, S. Gul, V.K. Yachandra, X. Hu, J. Yano, Evidence from in Situ X-ray Absorption Spectroscopy for the Involvement of Terminal Disulfide in the Reduction of Protons by an Amorphous Molybdenum Sulfide Electrocatalyst, Journal of the American Chemical Society, 137 (2015) 314-321.
[54] L. Wu, A. Longo, N.Y. Dzade, A. Sharma, M.M.R.M. Hendrix, A.A. Bol, N.H. de Leeuw, E.J.M. Hensen, J.P. Hofmann, The Origin of High Activity of Amorphous MoS2 in the Hydrogen Evolution Reaction, ChemSusChem, 12 (2019) 4383-4389.
[55] A. Zitolo, N. Ranjbar-Sahraie, T. Mineva, J. Li, Q. Jia, S. Stamatin, G.F. Harrington, S.M. Lyth, P. Krtil, S. Mukerjee, E. Fonda, F. Jaouen, Identification of catalytic sites in cobalt-nitrogen-carbon materials for the oxygen reduction reaction, Nature Communications, 8 (2017) 957.
[56] A. Filipponi, A. Di Cicco, C.R. Natoli, X-ray-absorption spectroscopy and n-body distribution functions in condensed matter. I. Theory, Physical Review B, 52 (1995) 15122-15134.
[57] A. Filipponi, A. Di Cicco, X-ray-absorption spectroscopy and n-body distribution functions in condensed matter. II. Data analysis and applications, Physical Review B, 52 (1995) 15135-15149.
[58] P.A. Lee, P.H. Citrin, P. Eisenberger, B.M. Kincaid, Extended x-ray absorption fine structure---its strengths and limitations as a structural tool, Reviews of Modern Physics, 53 (1981) 769-806.
[59] S.J. Hibble, D.A. Rice, D.M. Pickup, M.P. Beer, Mo K-edge EXAFS and S K-edge absorption studies of the amorphous molybdenum sulfides MoS4.7, MoS3, and MoS3.cntdot.nH2O (n .apprx. 2), Inorganic Chemistry, 34 (1995) 5109-5113.
[60] T. Weber, J.C. Muijsers, J.W. Niemantsverdriet, Structure of Amorphous MoS3, The Journal of Physical Chemistry, 99 (1995) 9194-9200.
[61] P.D. Tran, Thu V. Tran, M. Orio, S. Torelli, Q.D. Truong, K. Nayuki, Y. Sasaki, Sing Y. Chiam, R. Yi, I. Honma, J. Barber, V. Artero, Coordination polymer structure and revisited hydrogen evolution catalytic mechanism for amorphous molybdenum sulfide, Nature Materials, 15 (2016) 640-646.
[62] L.R.L. Ting, Y. Deng, L. Ma, Y.-J. Zhang, A.A. Peterson, B.S. Yeo, Catalytic Activities of Sulfur Atoms in Amorphous Molybdenum Sulfide for the Electrochemical Hydrogen Evolution Reaction, ACS Catalysis, 6 (2016) 861-867.
[63] S.P. Cramer, K.S. Liang, A.J. Jacobson, C.H. Chang, R.R. Chianelli, EXAFS studies of amorphous molybdenum and tungsten trisulfides and triselenides, Inorganic Chemistry, 23 (1984) 1215-1221.
[64] A.L. Lennie, D.J. Vaughan, Spectroscopic studies of iron sulfide formation and phase relations at low temperatures, Mineral Spectroscopy 5(1996) 117-131.
[65] A. Sahu, S.N. Steinmann, P. Raybaud, Size-Dependent Structural, Energetic, and Spectroscopic Properties of MoS3 Polymorphs, Crystal Growth & Design, 20 (2020) 7750-7760.
[66] J. Zhang, Y. Wu, H. Hao, Y. Zhang, X. Chen, K. Xing, J. Xu, Construction of amorphous Fe0.95S1.05 nanorods with high electrocatalytic activity for enhanced hydrogen evolution reaction, Electrochimica Acta, 402 (2022) 139554.
[67] G. Zhou, Y. Shan, L. Wang, Y. Hu, J. Guo, F. Hu, J. Shen, Y. Gu, J. Cui, L. Liu, X. Wu, Photoinduced semiconductor-metal transition in ultrathin troilite FeS nanosheets to trigger efficient hydrogen evolution, Nature Communications, 10 (2019) 399.

[68] L. Loh, Z. Zhang, M. Bosman, G. Eda, Substitutional doping in 2D transition metal dichalcogenides, Nano Research, 14 (2021) 1668-1681.
[69] S. Anantharaj, S.R. Ede, K. Sakthikumar, K. Karthick, S. Mishra, S. Kundu, Recent Trends and Perspectives in Electrochemical Water Splitting with an Emphasis on Sulfide, Selenide, and Phosphide Catalysts of Fe, Co, and Ni: A Review, ACS Catalysis, 6 (2016) 8069-8097.
[70] H. Wang, C. Tsai, D. Kong, K. Chan, F. Abild-Pedersen, J.K. Nørskov, Y. Cui, Transition-metal doped edge sites in vertically aligned MoS2 catalysts for enhanced hydrogen evolution, Nano Research, 8 (2015) 566-575.
[71] J. Guo, X. Zhang, Y. Sun, L. Tang, X. Zhang, NiMoS3 Nanorods as pH-Tolerant Electrocatalyst for Efficient Hydrogen Evolution, ACS Sustainable Chemistry & Engineering, 5 (2017) 9006-9013.
[72] P. Liu, J. Zhu, J. Zhang, K. Tao, D. Gao, P. Xi, Active basal plane catalytic activity and conductivity in Zn doped MoS2 nanosheets for efficient hydrogen evolution, Electrochimica Acta, 260 (2018) 24-30.

		Dry electrode			OCP			-0.21V vs RHE		
		R(Å)	$\sigma^2(10^{-3}$ Å$^2)$	CN	R(Å)	$\sigma^2(10^{-3}$ Å$^2)$	CN	R(Å)	$\sigma^2(10^{-3}$ Å$^2)$	CN
MoS_{mw}	Mo-S	2.37(1)	8.7(2)	3.5(3)	2.37(2)	8.8(3)	3.8(4)	2.37(2)	8.9(3)	4.7(5)
	Mo-Mo	2.76(1)	6.5(2)	0.7(1)	2.73(1)	9.5(5)	0.9(2)	2.77(1)	7.0(3)	0.9(1)
	Mo-O	1.68(2)	2.0(3)	0.2(1)	1.68(2)	1.5(5)	0.1(2)	-	-	-
$FeMoS_{mw}$	Mo-S	2.38(2)	9.7(5)	3.3(2)	2.37(1)	8.6(2)	3.9(3)	2.38(2)	8.3(3)	4.3(3)
	Mo-Mo	2.76(1)	5.7(3)	0.8(1)	2.74(1)	9.4(3)	1.6(3)	2.76(2)	9.0(3)	1.4(3)
	Mo-O	1.69(2)	1.5(4)	0.3(1)	-	-	-	-	-	-
MoS_3 (ex-situ)	Mo-S	2.42(1)	9.0(5)	5.6(3)	-	-	-	-	-	-
	Mo-Mo	2.77(1)	3.4(2)	0.8(2)	-	-	-	-	-	-

Table 1. Best-fit parameters obtained from the Mo K-edge EXAFS analysis of MoS_{mw} and $FeMoS_{mw}$ catalysts for the dry-electrode, at OCP and during catalytic conditions. MoS_3 parameters are also determined for the reference compound in the ex-situ form. R is the bond

distance, σ^2 is the Debye-Waller factor, and CN is the coordination number. Errors are given in parentheses, e.g. 2.37(1) means 2.36-2.38

		Dry electrode			OCP		
		R(Å)	$\sigma^2(10^{-3}$ Å$^2)$	CN	R(Å)	$\sigma^2(10^{-3}$ Å$^2)$	CN
$FeMoS_{(mw)}$	Fe-S	2.28(2)	1.0(2)	0.6(1)	2.25(1)	4.1(3)	2.7(2)
	Fe-Fe	2.86(2)	1.0(3)	0.6(2)	2.86(1)	2.6(3)	0.5(2)
	Fe-O	2.02(2)	5.0(5)	3.0(3)	-	-	-

Table 2. Best-fit parameters obtained from the Fe K-edge EXAFS analysis of $FeMoS_{mw}$ for the dry-electrode, and at OCP. R is the bond distance, σ^2 is the Debye-Waller factor, and CN is the coordination number. Errors are given in parentheses, e.g. 2.28(2) means 2.26-2.30

Figure Captions

Figure 1. Polarization curve for HER on MoS_{mw} and $FeMoS_{mw}$ electrocatalysts (catalyst loading: 0.82 mg·cm^{-2} 3rd scan). Conditions: N_2-saturated 0.1 M H_2SO_4, scan rate 5 mV·s^{-1}, Ti wire counter electrode. The black curve (on GC) and gray curve (on CNTs) are shown for comparison.

Figure 2. Structure of *a*-MoS_3 according to the model of (a) Hibble, (b) Weber, and (c) Artero.

Figure 3. Ex-situ Mo K-edge FT-EXAFS analysis of (a) MoS_{mw} and (b) $FeMoS_{mw}$. The black curves represent the experimental spectra, whereas the red curves represent calculated spectra.

Figure 4. *Operando* Mo K-edge XANES spectra of (a) MoS_{mw} and (b) $FeMoS_{mw}$. Spectra were measured in N_2-saturated 0.1 M H_2SO_4 electrolyte at OCP (blue lines), -0.21 V vs RHE (green lines), and compared with the spectra recorded on the dry electrodes (red lines).

Figure 5. Comparison between the Fe K-edge (a) XANES and (b) FT-EXAFS spectra of $FeMoS_{mw}$ on the dry electrode (red lines) and at OCP (blue lines).

Figure 6. Fe K-edge FT-EXAFS analysis of (a) $FeMoS_{mw}$ dry electrode and (b) $FeMoS_{mw}$ at OCP. The black curves represent the experimental spectra, whereas the red curves represent calculated spectra.

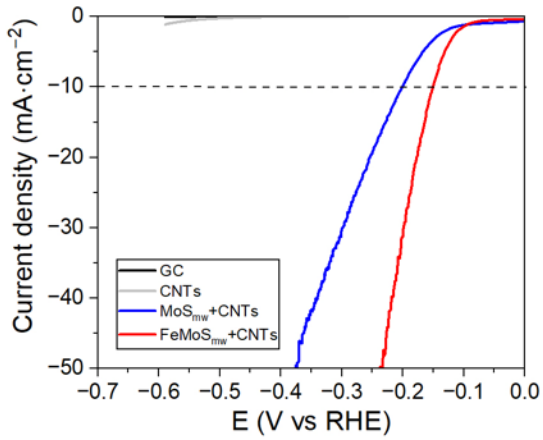

Fig1

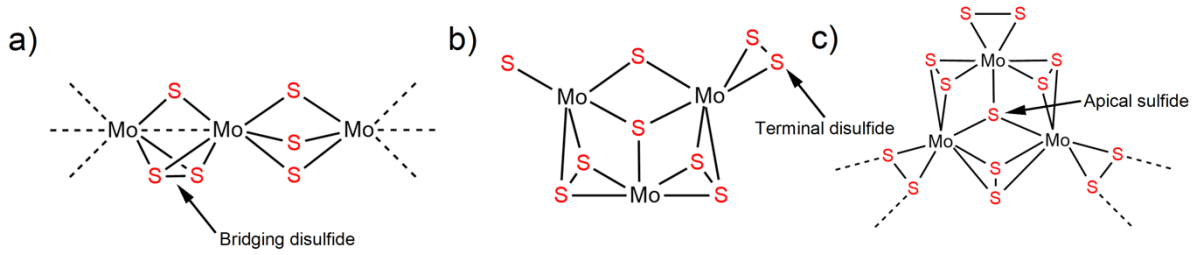

Fig2

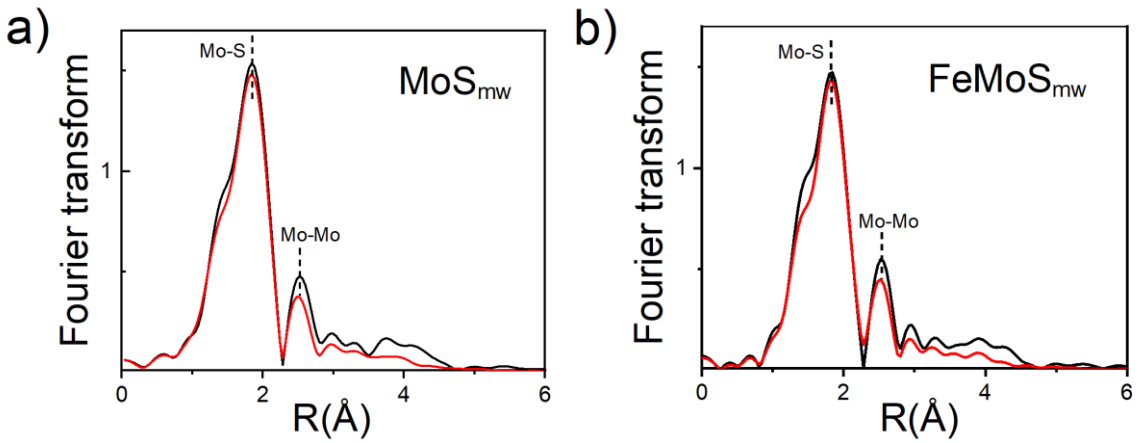

Fig3

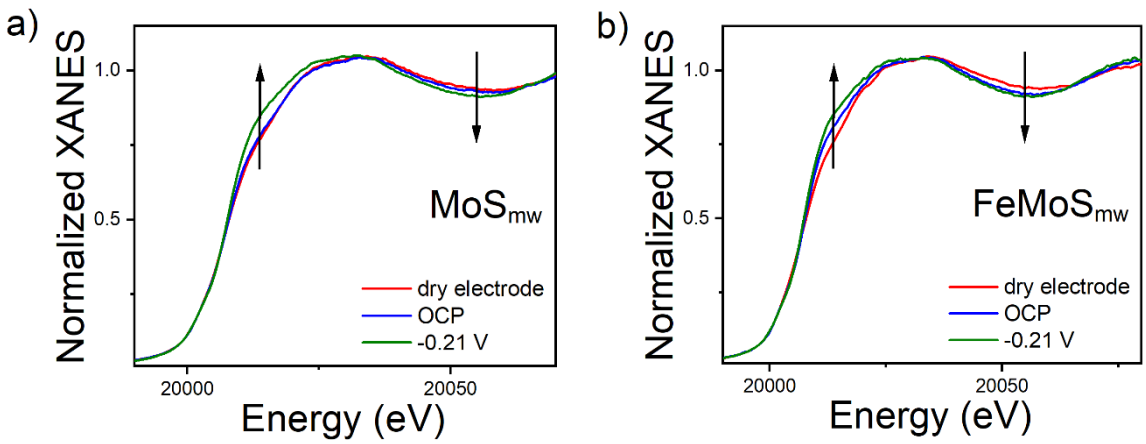

Fig4

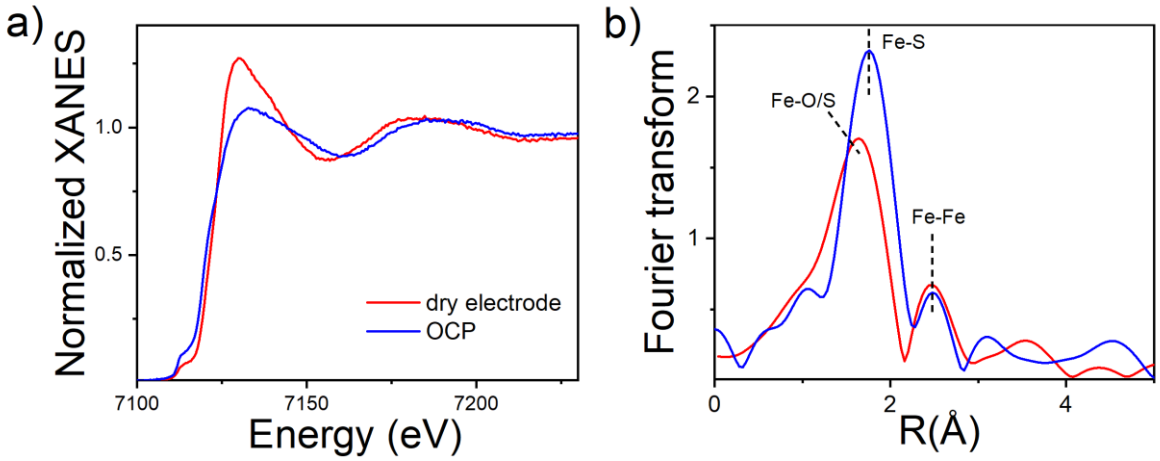

Fig5

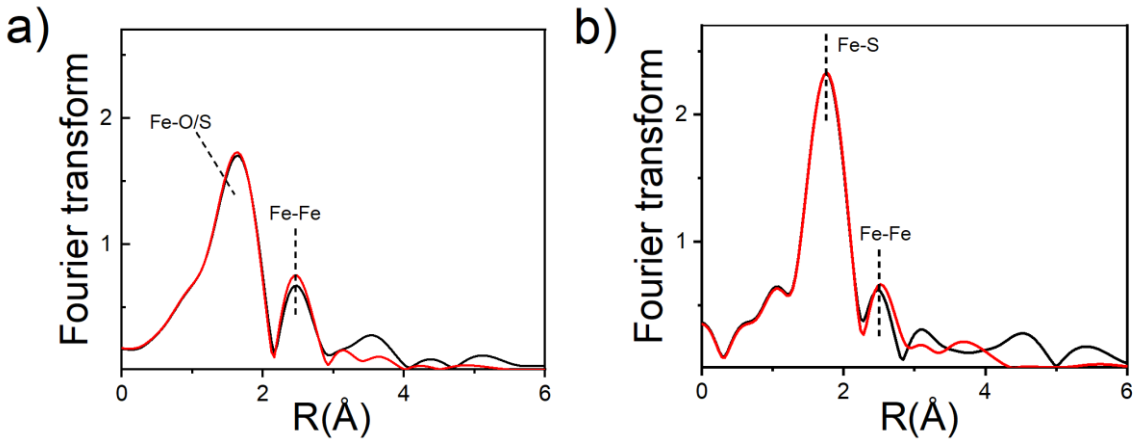
a)
Fourier transform
Fe-O/S
Fe-Fe
R(Å)
b)
Fourier transform
Fe-S
Fe-Fe
R(Å)

Fig6